Engineering Science and Technology, an International Journal 84 (2026) 102554

Contents lists available at ScienceDirect

Engineering Science and Technology, an International Journal

journal homepage: www.elsevier.com/locate/jestch

Full length article

Finite element analysis driven optimization of an electrodynamic levitation system with permanent magnet Halbach arrays

Erkan Caner Ozkat [a,c,*], Murat Abdioglu [b,c], U. Kemal Ozturk [c]

[a] Department of Mechanical Engineering, Faculty of Engineering and Architecture, Recep Tayyip Erdogan University, 53100, Rize, Turkey
[b] Department of Mathematics and Science Education, Faculty of Education, Bayburt University, 69000, Bayburt, Turkey
[c] Electromagnetic Guidance and Acceleration Research Group (EMGA), Department of Physics, Faculty of Science, Karadeniz Technical University, 61080, Trabzon, Turkey

ARTICLE INFO

Keywords:
Electrodynamic levitation system
Permanent magnet Halbach arrays
FEA modeling
Optimization
Lift and drag forces

ABSTRACT

This study presents a finite element analysis (FEA)-driven optimization for the design of an electrodynamic levitation (EDL) system incorporating permanent magnet Halbach arrays (PM-HAs). The primary objective is to maximize the net force difference between lift (F_y) and drag (F_x) forces under realistic physical and manufacturing constraints. The nonlinear electromagnetic behavior of the EDL system is modeled using high-fidelity FEA, capturing the complex interaction between the PM-HA and a conductive plate. At each iteration of the population-based optimization algorithm, full magnetoquasistatic simulations are performed to ensure a physically accurate evaluation of key performance metrics. A comprehensive parametric study involving 256 distinct PM-HA configurations reveals a non-monotonic relationship between the number of magnets and levitation performance, highlighting the critical role of magnetic field distribution. Configurations with 9 to 11 magnets achieve the highest net levitation force. The optimization results indicate that the optimal configuration includes four horizontally aligned permanent magnets (PMs) with a width of 74.00 mm and three vertically aligned PMs with a width of 74.67 mm, along with a 7 mm thick conductive plate having a conductivity of $5 \times \mathbf{10}^{7}$ S/m. This design delivers a maximum lift force of 3550 N and a minimum drag force of 279 N at 100 m/s. The findings demonstrate that effective EDL system design requires a carefully arranged magnet configuration rather than a simple maximization of magnet count or size. The proposed FEA-guided framework offers a robust and scalable methodology for the optimization of high-performance Maglev systems.

1. Introduction

Electrodynamic levitation (EDL) systems have become a promising technology for enabling contactless motion in high-speed maglev transportation. These systems utilize the principle of electromagnetic induction, where the relative motion between a moving magnetic field and a conductive surface generates eddy currents that produce a repulsive lift force. As the demand for efficient, low-maintenance, and high-performance levitation solutions increases, especially in environments where mechanical contact is undesirable or impractical, the development of robust EDL systems has gained critical importance.

Compared to other levitation technologies, such as electromagnetic levitation (EML) or conventional wheel-to-rail systems, EDL offers several inherent advantages [1,2]. The attraction of the EDL system lies in its ability to achieve self-stabilization, simplifying operational controls compared to EML-based solutions, aligning with a broader goal of creating more robust and reliable high-speed transit options and contactless operation [3–5]. Moreover, EDL systems employing Halbach arrays of permanent magnets (PMs) further enhance performance by concentrating magnetic flux on the levitation side while suppressing it on the opposite side [6–8]. This unique configuration not only improves levitation force but also minimizes drag force and thus energy losses, making Halbach-based EDL systems particularly attractive for advanced levitation applications [9].

Various studies have demonstrated the applicability of EDL systems in high-speed transportation systems. For instance, research indicates that EDL systems, operating under the principles of magnetic repulsion generated by induced eddy currents in conductive plate materials, can effectively support vehicles at high velocities with minimal mechanical guidance [10]. In addition, the use of hybrid levitation systems that combine permanent and electromagnetic magnets has been shown

* Corresponding author at: Department of Mechanical Engineering, Faculty of Engineering and Architecture, Recep Tayyip Erdogan University, 53100, Rize, Turkey.
E-mail address: erkancaner.ozkat@erdogan.edu.tr (E.C. Ozkat).

https://doi.org/10.1016/j.jestch.2026.102554
Received 29 January 2026; Received in revised form 27 August 2026; Accepted 25 September 2026
Available online 11 October 2026
2215-0986/© 2026 The Author(s). Published by Elsevier B.V. on behalf of Karabuk University. This is an open access article under the CC BY-NC-ND license (http://creativecommons.org/licenses/by-nc-nd/4.0/).

to significantly reduce power loss, thereby enhancing overall system efficiency [11]. More recently, three-dimensional models that explicitly capture the end effects of the onboard magnets have been employed to analyze and improve the dynamic behavior of PM EDL systems; in particular, the end effect of the onboard magnets has been exploited to enhance the passive damping characteristics of permanent magnet electrodynamic suspension vehicles [12,13]. While EDL systems offer many benefits, their effective design requires careful attention to the interactions between magnetic fields, induced currents, and system dynamics. Achieving optimal performance requires careful tuning of design parameters such as magnet geometry, magnetic pole arrangement, and structural and intrinsic properties of the conductive plate. Consequently, there is a growing need for systematic optimization frameworks that can capture the nonlinear electromagnetic behavior of EDL systems and guide the design process toward performance-enhancing configurations under realistic physical and manufacturing constraints.

Jiang et al. [14] explored the size optimization of Halbach arrays, demonstrating that an intelligently designed magnetic levitation system can significantly enhance the levitation force. This is particularly relevant in systems like the "Rainbow" maglev train, which utilizes real-time dynamic suspension adjustments to ensure safety and stability. Similarly, Deng et al. [15,16] emphasized the importance of optimizing the permanent magnet guideway (PMG) for high-temperature superconducting (HTS) Maglev systems, indicating that a well-optimized PMG can improve the carrying capacity and overall performance of the system. Yang et al. [17] conducted numerical simulations to analyze the stability of Maglev vehicles at various speeds, revealing that optimized suspension parameters can lead to improved dynamic responses. Ozkat et al. [18] developed a novel optimization framework to identify geometric parameters of the levitation system that maximize levitation while ensuring lateral force remains within a defined tolerance in HTS Maglev systems. Talukdar & Talukdar [19] corroborated this by demonstrating that optimized suspension parameters could reduce vertical acceleration and guideway deflection significantly.

These findings underscore the necessity of a comprehensive approach to modeling and optimization in Maglev systems. Simulation and modeling techniques are vital for testing and refining these optimization strategies. For example, the use of virtual prototypes and surrogate or machine/deep learning models allows researchers to simulate the dynamics of the suspension system under different configurations, leading to improved ride quality and stability [20–23]. Additionally, the application of intelligent algorithms, such as particle swarm, genetic algorithm, ant colony and differential evolution optimizations, has proven effective in fine-tuning suspension parameters to achieve desired performance metrics [24–27].

Although previous optimization studies have investigated some aspects of Maglev system optimization, such as improving PMGs in HTS systems or tuning suspension parameters for better ride quality, most have not focused specifically on EDL systems using PM-HAs. Furthermore, some research in the literature focused on the numerical and analytical simulation studies on permanent magnet-conductive plate systems considering limited parameters such as conductive plate thickness, wavelength and fill factor of the permanent magnetic array (PMA) [8,9,28]. There is a noticeable gap in the literature regarding efforts to optimize the force difference between lift and drag forces under realistic physical and manufacturing constraints. Addressing this objective is essential, as improving the lift-to-drag ratio (LDR) not only enhances the levitation efficiency and dynamic stability of EDL systems but also contributes to more compact, energy-efficient, and economically viable designs suitable for real-world applications.

To address this need, the objective of this study is to conduct the finite element analysis (FEA)-driven optimization approach for the design of an EDL system using the permanent magnet Halbach arrays (PM-HAs) to accurately capture the complex, nonlinear electromagnetic interactions between the Halbach array and the conductive track, which are difficult to approximate reliably with surrogate or machine learning models. Thus, electromagnetic behavior of the PM-HA based EDL system is analyzed in detail with FEA, and the results of these analyses drive the optimization process. The objective function of the optimization is to maximize the force difference between the lift force and the drag force acting between the conductive plate and the PM-HA, subject to the total length of the PM-HA (l_{PM-HA}) must remain within a specified range to satisfy spatial design limits, to preserve the magnetic field configuration characteristic of Halbach arrays and all design parameters.

The remainder of this paper is organized as follows: Section 2 presents the methodology, including the FEA framework developed for modeling the electrodynamic levitation system and the formulation of the constraint optimization problem. Section 3 discusses the results obtained from the simulation-based optimization process and analyzes their implications in terms of system performance. Finally, Section 4 summarizes the key conclusions and outlines potential directions for future research.

2. Methodology

This study employs a comprehensive FEA framework to investigate and optimize the electromagnetic performance of a Maglev system based on the PM-HA and conductive plate interaction. The model geometry consists of linearly arranged PMs levitated above the conductor, with a surrounding air domain (See Fig. 1) included to ensure accurate field resolution. Electromagnetic behavior was governed by the magnetoquasistatic approximation of Maxwell's equations, with the Lorentz force derived from induced eddy currents as the primary performance metric.

The electromagnetic behavior of the PM-HA based EDL system is rigorously analyzed using high-fidelity FEA, and the results of these simulations directly drive the optimization process. At each iteration of the population-based optimization algorithm, a complete FEA solution is executed according to the proposed methodology. The modeling framework is carefully configured to emulate realistic physical conditions by incorporating detailed material definitions, accurate boundary conditions, and mesh refinement strategies tailored to electromagnetic field resolution. Key performance metrics such as lift force, drag force, the difference between lift and drag forces and LDR are governed by highly nonlinear, spatially varying, and field-coupled interactions that cannot be reliably captured by low-fidelity surrogate or machine learning-based models. While data-driven approaches can approximate the output values rapidly, they typically provide limited insight into the underlying physical mechanisms. In contrast, FEA-based models not only yield quantitative predictions but also emulate the full electromagnetic response of the system, including current distributions, magnetic vector potential and magnetic flux density. For this reason, high-fidelity FEA solutions were employed throughout the optimization process to ensure both the physical accuracy and the interpretability of the design space exploration.

2.1. Finite element analysis for the Maglev system

To analyze the electromagnetic force characteristics of the Maglev system, a 2D FEA was constructed using COMSOL Multiphysics 6.1, incorporating the AC/DC Module and the Rotating Machinery, Magnetic (RMM) physics interface. In this model, the relative motion between the maglev wagon, containing the PM-HA, and the conductive plate is represented by assigning an increasing translational velocity (v_x) from 0 m/s to 100 m/s to the plate. This motion is incorporated through the Lorentz force term within RMM physics interface in COMSOL Multiphysics 6.1.

To systematically evaluate the influence of geometric and material design parameters on the resulting lift and drag forces, a comprehensive parametric study was conducted. This involved 256 unique

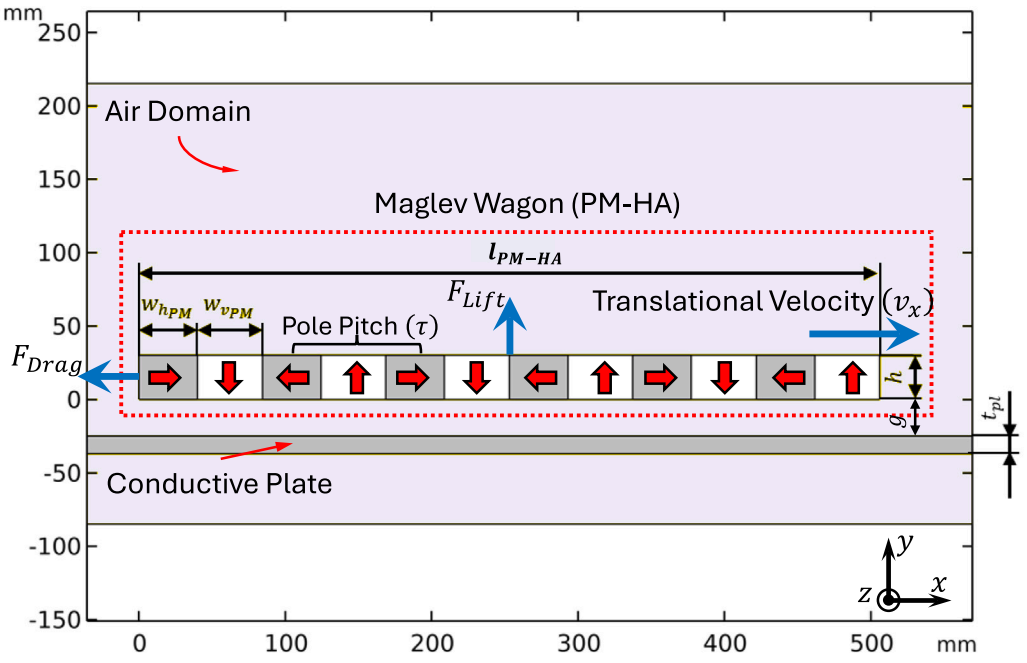


Fig. 1. The geometrical model of the Maglev system. Arrows on the PMs indicate the magnetization directions.

Table 1
Discrete design levels used in the parametric study.

Design parameters	Symbols	Unit	Levels
Conductive plate thickness	t_{pl}	mm	2,5,8,12
Horizontal PM width	$w_{h_{PM}}$	mm	25, 30, 35, 40
Vertical PM width	$w_{v_{PM}}$	mm	[13.3 ↔ 222.5]
Electrical conductivity of the plate	σ	S/m	2, 3, 4, 5 $\times 10^7$
Number of horizontal PMs	$n_{h_{PM}}$	–	3, 4, 5, 6, 7, 8, 9, 10
Number of vertical PMs	$n_{v_{PM}}$	–	2, 3, 4, 5, 6, 7, 8, 9

simulation cases, each defined by a distinct combination of conductive plate thickness (t_{pl}), permanent magnet dimensions ($w_{h_{PM}}$), ($w_{v_{PM}}$), the electrical conductivity of the plate (σ), and the number of permanent magnets (n_{PM}) oriented both horizontally ($n_{h_{PM}}$) and vertically ($n_{v_{PM}}$) in the PM-HA. The complete set of design parameters is summarized in Table 1. In this study, l_{PM-HA} was kept constant at 520 mm, $w_{h_{PM}}$, $n_{h_{PM}}$ and $n_{v_{PM}}$ were selected according to Table 1, and $w_{v_{PM}}$ was computed in the range of 13.3 mm to 222.5 mm. The modeling framework is configured to emulate realistic physical conditions by incorporating accurate material definitions, boundary conditions, and meshing strategies. Detailed descriptions of model geometry, material assignments, physical interfaces, and solver settings are provided in the following sections.

2.1.1. Geometric configuration

The geometric configuration of the model represents a two-dimensional cross-section of the PM-HA magnetic levitation system as illustrated in Fig. 1. The setup consists of linearly arranged Halbach array of rectangular PMs positioned above a horizontally translating conductive plate. The Halbach array is a special arrangement in which some of the PMs are magnetized horizontally (h_{PM}) and some vertically (v_{PM}). While the PM height (h) is kept constant at 30 mm, the widths range from 25 mm to 40 mm for the horizontally oriented magnets and from 13.3 mm to 222.5 mm for the vertically oriented magnets. The total length of the PM-HA, which comprises horizontally and vertically arranged PMs, was kept constant at 520 mm. Therefore, the number of magnets varies from 5 to 19 depending on the configuration. In addition, the conductive plate is placed at a fixed air gap of 25 mm below the PM-HA and is modeled with a variable thickness between 2 mm and 12 mm. A sufficiently large surrounding air domain is included to ensure accurate electromagnetic field decay and to minimize boundary effects (See Fig. 1). This parametric geometry was automatically updated to evaluate the influence of each design variable on the resultant electromagnetic forces.

2.1.2. Governing physics and force calculation

The FEA model is based on the magnetoquasistatic form of Maxwell's equations and uses the magnetic vector potential formulation. Eqs. (1)–(3) relate the magnetic field intensity H to the current density J and enforce the divergence-free condition of the magnetic field. The induced current J is described in Eq. (4) by the Lorentz term in the RMM interface, which accounts for both the conductive and the motional components of the electric field.

$$\nabla \times \mathbf{H} = \mathbf{J} \tag{1}$$

$$\nabla \times \mathbf{A} = \mathbf{B} \tag{2}$$

$$\nabla \cdot \mathbf{B} = 0 \tag{3}$$

$$\mathbf{J} = \sigma \left(\mathbf{E} + \vec{v} \times \mathbf{B} \right) \tag{4}$$

The computational model consists of three principal domains: the PM-HA, the conductive plate, and the surrounding air region. The air domain is essential for accommodating magnetic field decay and minimizing the boundary effects. All external boundaries of the air region are assigned magnetic insulation conditions ($\mathbf{n} \cdot \mathbf{B} = 0$), which enforce tangential magnetic fields and emulate an open, non-reflective environment. At the interfaces between different materials, namely air, PM-HA, and conductor, standard electromagnetic continuity conditions are inherently satisfied by the finite element formulation, preserving the continuity of tangential magnetic field intensity and normal magnetic flux density.

The surrounding regions are modeled as air, applied to all domains not occupied by solid components as shown in Fig. 1. The remanent flux density (B_r) of each magnet in PM-HA is taken as 1.3 T and the relative permeability (μ_r) of the air medium and the conductive plate is taken

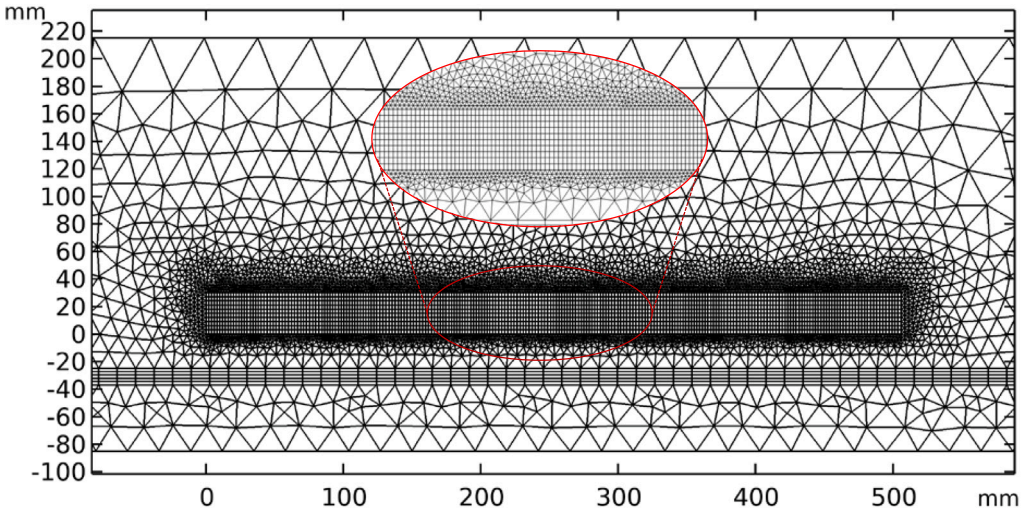


Fig. 2. Mesh structure of the FEA model.

as 1. The eddy currents are created in the conductive plate beneath the PM-HA as a result of the relative motion between the magnetic field source and the conductive plate. These eddy currents interact with the magnetic field of the PM-HA to generate Lorentz forces, which manifest as lift (F_L) and drag (F_D) acting on the plate.

The electromagnetic force components are computed by expressions for the F_L and F_D forces generated during relative motion between the PM array and the conductive plate. These forces are a function of system geometry, material properties, magnetic pole direction, and the translational velocity of the levitating body. The F_L and F_D are expressed as:

$$F_y = F_L = \frac{B_0^2 w \rho \tau}{\mu_0} \frac{1}{\beta\eta + 1} e^{-2\beta g} \tag{5}$$

$$F_x = F_D = \frac{B_0^2 w \rho \tau}{\mu_0} \frac{\beta\eta}{\beta\eta + 1} e^{-2\beta g} \tag{6}$$

where B_0 denotes the peak magnetic flux density of the PM array, w is the width of the magnet array, ρ is the number of pole pairs, and τ is the pole pitch (see Fig. 1). The magnetic field decay factor is characterized by $\beta = \pi/\tau$, and g represents the air gap between the PM-HA and the conductive plate and μ_0 is the vacuum permeability. A critical parameter in these equations is the skin depth (η), which governs the penetration of the magnetic field into the conductive plate, given by Eq. (7), where λ is the magnetic pole wavelength.

$$\eta = \sqrt{\frac{\lambda}{\pi \mu \sigma v_x}} \tag{7}$$

2.1.3. Meshing and solver strategy

A mapped mesh was applied to the conductive plate domain, discretized into 300 elements along the horizontal (x) direction and 5 elements along the vertical (y) direction to ensure sufficient resolution. Similarly, the PM-HA domain was meshed using a mapped mesh approach with 20 and 10 divisions along the x and y directions, respectively. For the surrounding air domain, a free triangular mesh was employed, with the minimum and maximum element sizes set to 0.309 mm and 82.5 mm, respectively, to balance computational efficiency and accuracy in capturing the electromagnetic field distribution. The total meshed area is approximately 1.208×10^6 mm^2. The mesh configuration for a specific simulation case which consists of 6 horizontal PMs and 6 vertical PMs, is illustrated in Fig. 2.

The electromagnetic problem was solved using a standard stationary solver appropriate for steady-state conditions. Given the increasing translational velocity of the moving conductor and the absence of time-varying sources, a magnetoquasistatic approximation was adopted. The system of equations was discretized using quadratic Lagrange elements and solved using a direct linear solver (PARDISO), which is well-suited for handling large, sparse systems arising from finite element formulations. Solver convergence was controlled via tight relative and absolute tolerances to ensure the accuracy of field and force predictions.

Table 2
Continuous lower and upper limits used in the optimization.

Design parameters	Symbols	Unit	Lower limit	Upper limit
Conductive plate thickness	t_{pl}	mm	5	8
Horizontal PM width	$w_{h_{PM}}$	mm	13.3	222.5
Vertical PM width	$w_{v_{PM}}$	mm	13.3	222.5
Electrical conductivity of the plate	σ	S/m	2×10^7	5×10^7
Number of horizontal PMs	$n_{h_{PM}}$	–	3	10
Number of vertical PMs	$n_{v_{PM}}$	–	2	9

2.2. The formulation of optimization problem

To enhance the electromagnetic performance of the Maglev system, the design problem is formulated as a constrained optimization problem with the aim of maximizing the force difference between F_y and F_x forces generated between the conductive plate and the PM-HA. The optimization is subject to a set of practical and physical constraints. The first constraint ensures that l_{PM-HA}, which is defined in Eq. (8), is fixed at 520 mm.

$$l_{\text{PM-HA}} = w_{h_{\text{PM}}} \times n_{h_{\text{PM}}} + w_{v_{\text{PM}}} \times n_{v_{\text{PM}}} \tag{8}$$

The second constraint addresses the structural and magnetic field configuration, requiring that the number of horizontally oriented PMs exceeds the number of vertically oriented PMs by at least one. This condition is imposed to satisfy the design principles of Halbach magnet arrays. Finally, a discrete constraint is imposed on the width of the horizontally oriented PMs to ensure manufacturability and compatibility with standard sizing, requiring that the width is always an integer. Furthermore, it should be emphasized that all design parameters were bounded with their lower limits (LL) and upper limits (UL), given in Table 2, to ensure their feasibility within the optimization process. Within this context, the optimization problem is mathematically formulated as:

$$\text{maximize} \quad F_y - F_x = f(t_{pl}, w_{h_{\text{PM}}}, w_{v_{\text{PM}}}, n_{h_{\text{PM}}}, n_{v_{\text{PM}}}, \sigma) \tag{9a}$$

$$\text{subject to} \quad l_{\text{PM-HA}} = 520 \text{ mm} \tag{9b}$$

$$n_{h_{\text{PM}}} = n_{v_{\text{PM}}} + 1 \tag{9c}$$

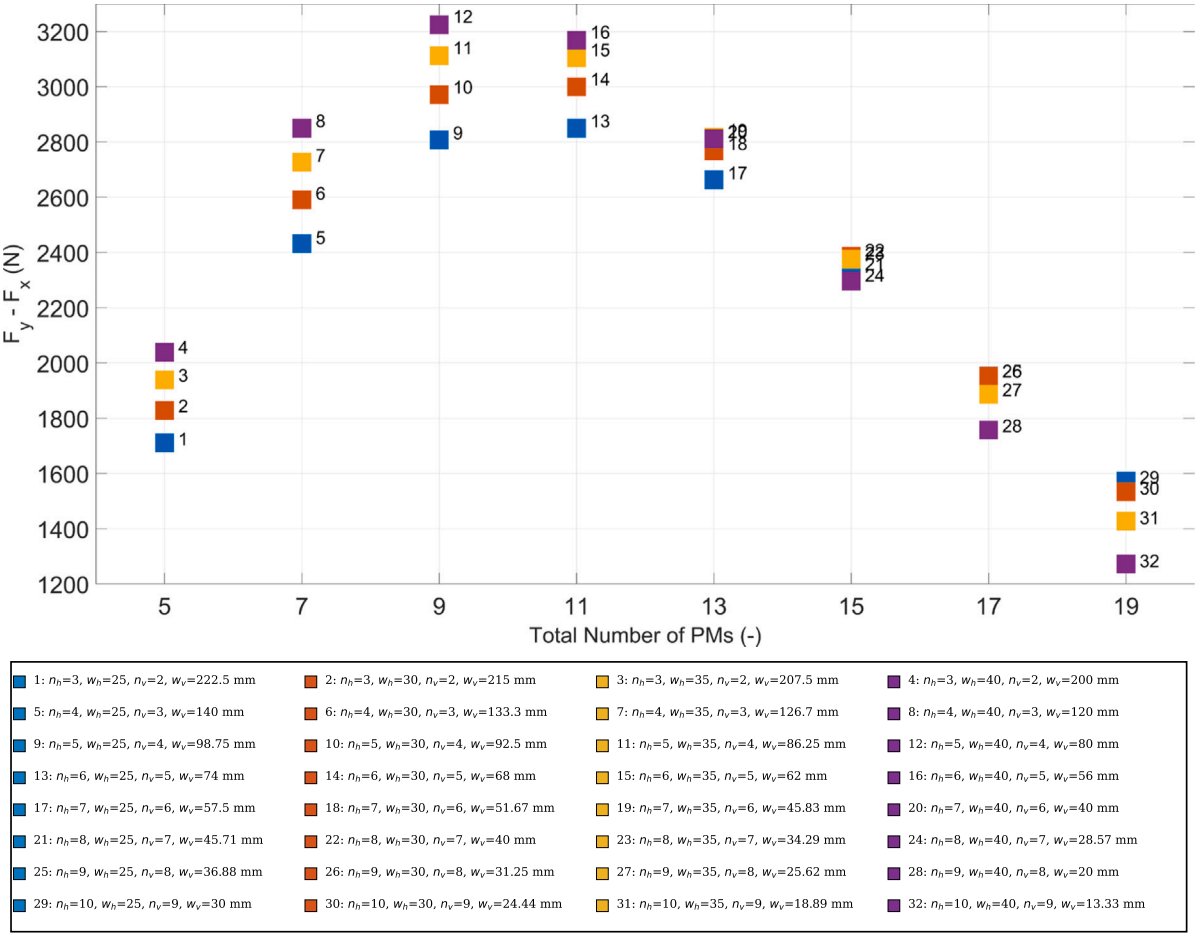


Fig. 3. Variation of the difference between lift force (F_y) and drag force (F_x) at the maximum translational velocity of 100 m/s as a function of the n_{PM} for various PM-HA configurations.

$$w_{h_{\mathrm{PM}}} \in \mathbb{Z}^{+} \tag{9d}$$

$$t_{pl}^{LL} \le t_{pl} \le t_{pl}^{UL} \tag{9e}$$

$$w_{h_{\mathrm{PM}}}^{LL} \le w_{h_{\mathrm{PM}}} \le w_{h_{\mathrm{PM}}}^{UL} \tag{9f}$$

$$w_{v_{\mathrm{PM}}}^{LL} \le w_{v_{\mathrm{PM}}} \le w_{v_{\mathrm{PM}}}^{UL} \tag{9g}$$

$$\sigma^{LL} \le \sigma \le \sigma^{UL} \tag{9h}$$

$$n_{h_{\mathrm{PM}}}^{LL} \le n_{h_{\mathrm{PM}}} \le n_{h_{\mathrm{PM}}}^{UL} \tag{9i}$$

$$n_{v_{\mathrm{PM}}}^{LL} \le n_{v_{\mathrm{PM}}} \le n_{v_{\mathrm{PM}}}^{UL} \tag{9j}$$

In this study, the Grey Wolf Optimization (GWO) algorithm, which is a population-based, nature-inspired metaheuristic optimization technique, was employed as the optimization strategy due to its proven effectiveness in solving complex, nonlinear engineering problems [29–32]. The GWO algorithm simulates the social dominance hierarchy of grey wolves, which iteratively updates the positions of candidate solutions by mimicking the encircling and hunting strategies observed in grey wolf packs, with the alpha wolf representing the best-known solution. A key feature of GWO is its balance between exploration and exploitation, achieved by the dynamic adjustment of control parameters over the course of iterations. Specifically, population size, which is the number of grey wolves (solution candidates) in the population, maximum Iterations, which is the total number of generations allowed, coefficient vectors, which are dynamic parameters that control the direction and distance of movement were chosen as 100, 300, and coefficient vectors reduced linearly from 2 to 0 over the iterations, respectively.

3. Results & discussions

3.1. Mesh independence

Before discussing the performance and optimization results, the mesh resolution used throughout the parametric study and the optimization is verified. A mesh independence study was carried out at the configuration with the highest $F_y - F_x$ in the parametric set (configuration 12 of Fig. 3) at the maximum translational velocity $v_x = 100$ m/s. This operating point combines the smallest in-plate skin depth of the entire study with the strongest concentration of the induced current density J_z at the upper surface of the conductor, and is therefore the most demanding case for mesh resolution.

Seven mesh levels were generated by global refinement, spanning two orders of magnitude in element count from 2873 to 430,843 domain elements (degrees of freedom from 7310 to over 500,000) and wall-clock solution times from 11 s to 2133 s. The complete results are reported in Table 3. Relative to the finest mesh (430,843 elements), the original mesh used throughout the parametric and optimization studies (13,659 elements, 33,492 degrees of freedom, 33 s per evaluation) deviates by −1.32% on F_y, −0.68% on F_x, and −1.73% on $F_y - F_x$. The convergence is monotone from the original mesh onward, and the variation between the second-finest mesh (147,418 elements) and the finest mesh is below 0.16% on every reported quantity. The original mesh therefore resolves the eddy-current distribution at the upper surface of the conductor with sub-2% accuracy, which is well below the magnitude of the parametric trends reported in the following subsections.

Table 3
Mesh independence study at configuration 12 ($n_{h_{PM}}$ = 5, $n_{v_{PM}}$ = 4, $w_{h_{PM}}$ = 40 mm, $w_{v_{PM}}$ = 80 mm, t_{pl} = 7 mm, $\sigma = 5 \times 10^7$ S/m) at v_x = 100 m/s. The row marked in bold is the mesh used throughout the parametric and optimization studies. Deviations are computed relative to the finest mesh (row 7).

Level	Elements	Boundary	DoF	Time (s)	F_y (N)	F_x (N)	$F_y - F_x$ (N)
1	2873	493	7310	11	3600.4	1357.0	2243.4
2	3473	603	9020	14	3509.5	1393.8	2115.7
3	5263	775	13,410	27	3520.6	1401.4	2119.2
4	**13,659**	**1,395**	**33,492**	**33**	**3536.4**	**1410.6**	**2125.8**
5	53,645	2753	143,735	167	3575.1	1418.8	2156.3
6	147,418	5164	401,557	630	3579.3	1419.5	2159.8
7	430,843	9793	1,285,400	2133	3583.6	1420.3	2163.3
Original mesh (level 4) vs. finest mesh:					−1.32%	−0.68%	−1.73%

The wall-clock cost of the finest mesh (2133 s per evaluation) is approximately 65× the cost of the original mesh (33 s per evaluation). A direct use of the finest mesh inside the GWO loop, which evaluates the objective function approximately $100 \times 300 = 30{,}000$ times, would have required approximately $30{,}000 \times 2133$ s ≈ 741 days of wall-clock time on the same hardware, which is not feasible. The original mesh is therefore the correct operating point for the parametric and optimization studies, with a sub-2% accuracy penalty relative to the converged solution.

3.2. Finite element analysis based performance evaluation

Fig. 4 presents the z-component of the current density (J_z) and the magnetic vector potential (A_z) in the conductive plate of an ELS featuring a PM–HA of fixed length at 520 mm under three different translational velocities (v_x): 0 m/s (stationary), 50 m/s, and 100 m/s. In this configuration, PMs set as follows: $n_{h_{PM}} = 5$, $n_{v_{PM}} = 4$, $w_{h_{PM}} = 35$ mm, $w_{v_{PM}}$ = 86.25 mm. The penetration depths of the eddy current (i.e. skin depths), denoted as η_1 and η_2, are also highlighted by red ellipses in 4(b) and Fig. 4(c) to visualize how electromagnetic skin effects evolve with the v_x. In the stationary case (See Fig. 4(a)), there is no induced eddy currents due to the absence of relative motion between the PM–HA and the conductive plate. The surface plot shows that J_z remains zero, and the A_z contour lines are tightly confined and symmetrical, indicating a localized magnetic field with limited interaction with the conductive medium. When the v_x increases to 50 m/s (See Fig. 4(b)), the eddy currents start to form in the conductive plate.

As v_x increased from 50 m/s to 100 m/s in Fig. 4(c), the maximum value of J_z increased from 1.51×10^8 A/m^2 to 2.21×10^8 A/m^2, respectively, indicating strong electromagnetic induction depending on the relative increase v_x between the PM–HA and the conductive plate. By comparing Fig. 4(b) and Fig. 4(c), it can be seen that the η_2 is thinner than η_1, highlighting that the increased v_x intensifies the skin effect, forcing eddy currents to become even more surface-bound. As described in Eqs. (5)–(7), an increase in the v_x leads to a reduction in the η, owing to their inverse relationship. This reduction in η enhances F_y while simultaneously diminishing F_x, as the induced eddy currents become more concentrated near the surface of the conductive plate. This thinning in η is crucial for system optimization, as it influences the design of the conductor thickness and material to balance between lift generation and resistive losses.

Fig. 5 demonstrates the effect of varying the horizontal and vertical numbers of permanent magnets ($n_{h_{PM}}$ and $n_{v_{PM}}$) on the distributions of the current density component J_z (surface plots) and the magnetic vector potential A_z (contour plots) within the conductive plate of the EDL system. In all cases, the translational velocity is fixed at v_x = 100 m/s, and the total PM–Halbach array length is maintained at 520 mm.

As shown in Fig. 5(a), for the lowest magnet configuration ($n_{h_{PM}}$ = 3, $n_{v_{PM}}$ = 2), the magnetic vector potential penetrates deeper into the conductive plate, resulting in eddy currents that are spatially broader and fewer in number. When the number of magnets is increased to $n_{h_{PM}}$ = 5 and $n_{v_{PM}}$ = 4 (Fig. 5(b)), the magnetic field becomes more confined to the surface region of the conductive plate, and the induced current density is concentrated into a smaller area directly beneath the PM array.

For the highest configuration, shown in Fig. 5(c) ($n_{h_{PM}}$ = 10, $n_{v_{PM}}$ = 9), the eddy current loops are highly localized near the surface, and the A_z contours exhibit densely packed patterns, indicating a strongly confined magnetic field. This progressive localization suggests a reduction in effective magnetic coupling with the conductive plate, leading to a less efficient utilization of the magnetic field for eddy current generation.

Fig. 5(d) presents the variation of the magnetic flux density (B) on the surface of the conductive plate (indicated by the red dashed line) along the length of the PM–HA array. The lowest n_{PM} exhibits fewer and broader peaks, indicating a low spatial frequency of the magnetic source, reaching a peak value of approximately 0.5 T. Increasing n_{PM} up to 9 increases the number of peaks and results in more localized variations in the magnetic field, with a reduced maximum flux density of approximately 0.42 T. The configuration with n_{PM} = 19 demonstrates the highest spatial frequency, with many small and sharp peaks; however, the maximum value decreases further to approximately 0.26 T. This reduction is attributed to magnetic field interference and partial cancellation effects due to the close proximity of neighboring magnets.

The trend observed in the magnetic flux density correlates with changes in the J_z. Specifically, the J_z value increases from 1.58×10^8 A/m^2 to 2.21×10^8 A/m^2, with a moderate increase in the n_{PM}, indicating stronger magnetic interaction. However, as the n_{PM} further increases to 19, the J_z value decreases to 2.01×10^8 A/m^2, suggesting that the average magnitude of magnetic flux per unit area becomes more predominant than the peak intensity.

The force results corresponding to the PM–HA configurations depicted in Fig. 5(a)–(c) are evaluated and presented in Fig. 6. These results, obtained using the FEA described in the methodology section, show the variation of lift (F_y) and drag (F_x) forces as a function of v_x, increasing from 0 to 100 m/s. The force profiles reflect the influence of different magnet arrangements on the electromagnetic performance, highlighting how configuration changes affect both levitation and resistive behavior across the velocity range. In all cases, F_y rapidly increases at lower speeds and begins to saturate as the velocity increases; meanwhile, F_x rises initially, reaches a peak at low velocities, and then gradually decreases with increasing the v_x. The observed trends are closely tied to the magnetic characteristics of the configurations, as clarified in Fig. 5(d). Specifically, an increase in the n_{PM} leads to a decrease in the peak magnetic flux density (B_0), as described by Eqs. (5) and (6).

Fig. 7 presents the variation in the F_y generated by different PM-HA configurations as a function of the n_{PM}, evaluated at the maximum v_x value of 100 m/s. Each data point represents a distinct PM-HA configuration. The figure reveals a non-monotonic relationship between the F_y and the n_{PM}. An initial increase in F_y is observed with an increasing n_{PM}, reaching a maximum at 9 and 11 PMs.

As shown in Eq. (5), the F_y is proportional to the square of the magnetic flux density. Fig. 5(d) demonstrates that the average magnetic flux density for the configuration with $n_{PM} = 9$ is higher than those for

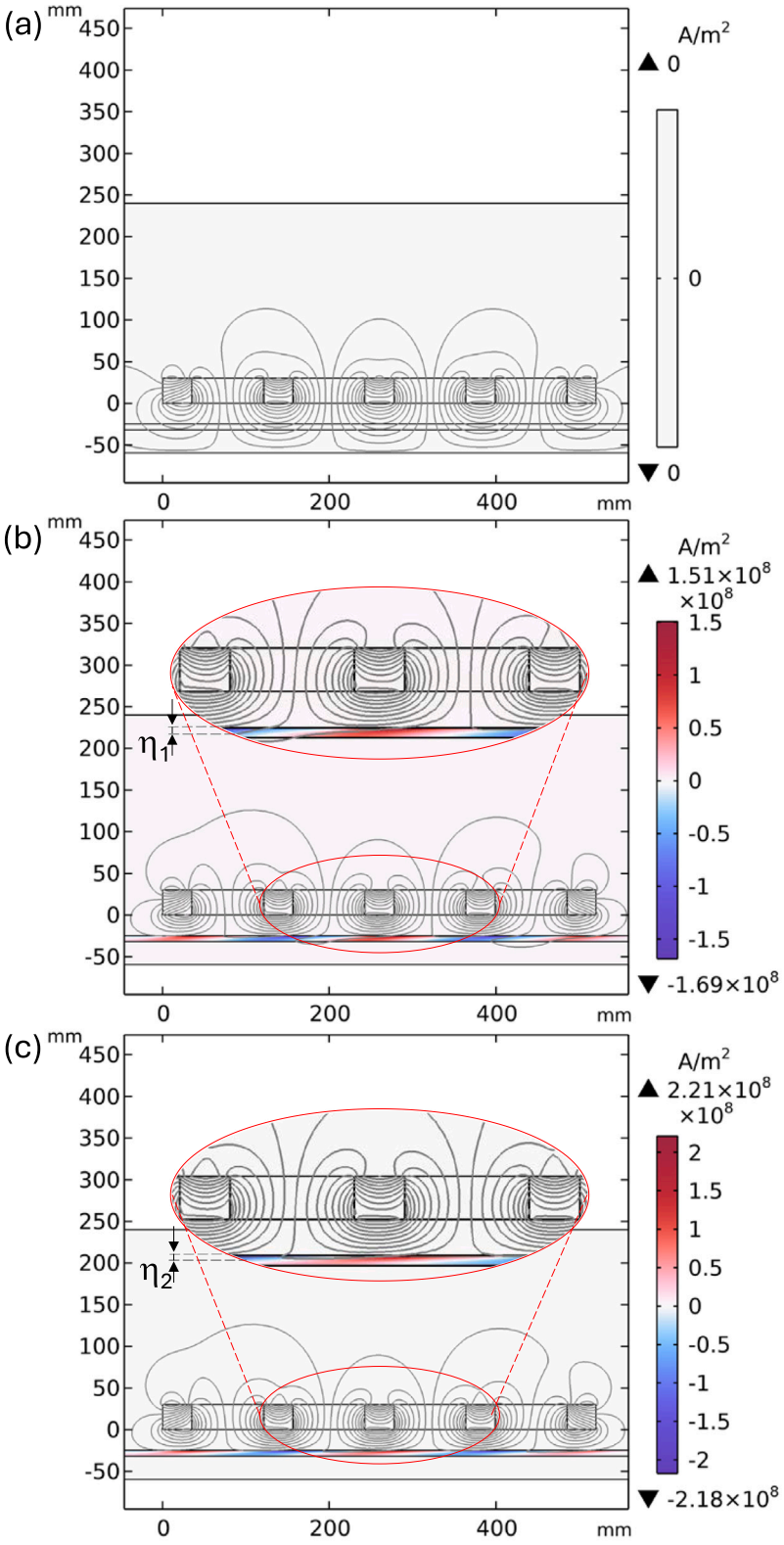


Fig. 4. z-component of the current density (J_z) in the conductive plate and magnetic vector potential (A_z) under different motion conditions: (a) at stationary state, (b) with a translational velocity of 50 m/s, and (c) 100 m/s. The PM–HA length is fixed at 520 mm with $n_{h_{PM}} = 5$, $n_{v_{PM}} = 4$, $w_{h_{PM}} = 35$ mm, $w_{v_{PM}} = 86.25$ mm. Surface plot shows the z-component of the current density while contour plot shows the z-component of the magnetic vector potential.

$n_{PM} = 5$ and $n_{PM} = 19$. In addition, the $n_{PM} = 9$ configuration exhibits three dominant flux density peaks, whereas the $n_{PM} = 5$ configuration shows only a single peak, and the $n_{PM} = 19$ configuration displays a plateau-like distribution around 0.22 T. Therefore, this more favorable flux distribution of the $n_{PM} = 9$ configuration, relative to the other cases, results in its higher levitation force.

Fig. 3 illustrates the variation of $F_y - F_x$ as a function of the n_{PM} at $v_x = 100$ m/s. For configurations with $n_{PM} = 5$, $n_{PM} = 9$, and

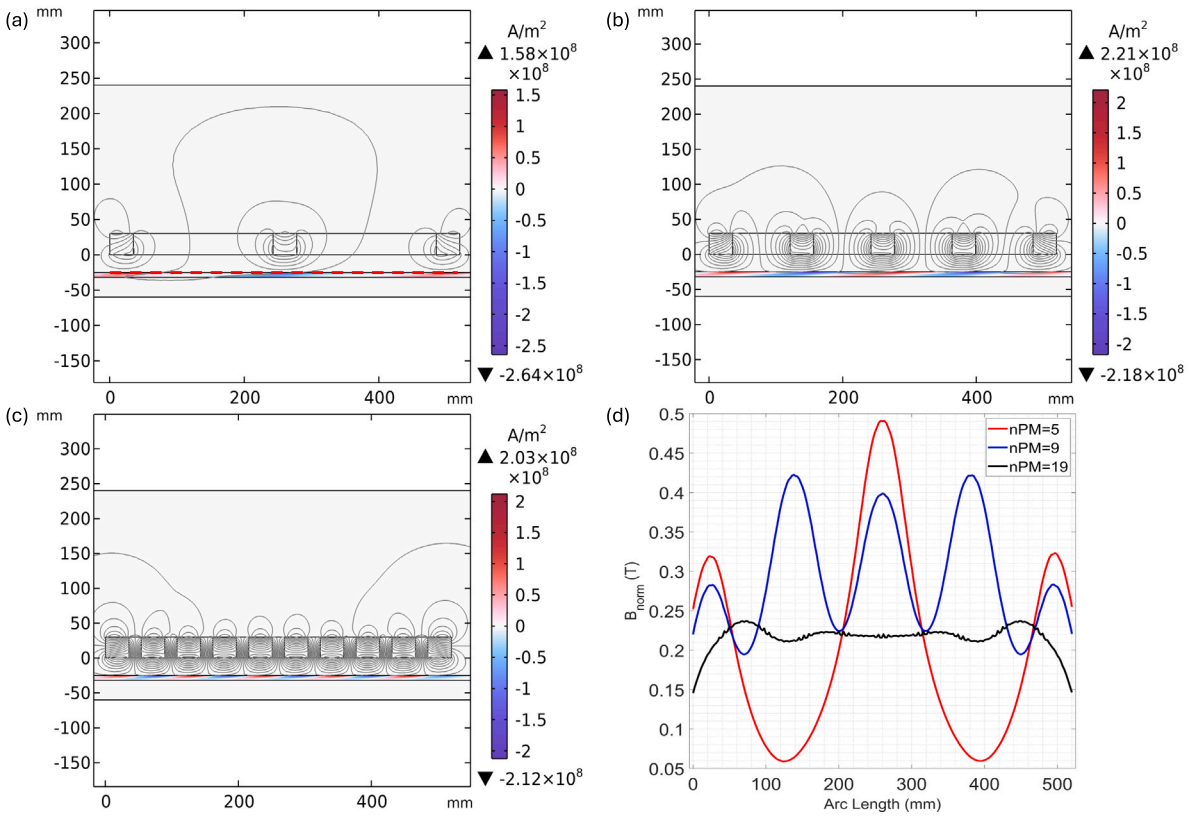


Fig. 5. z-component of the current density (J_z: surface plot) in the conductive plate and magnetic vector potential (A_z: contour plot) for varying configurations of horizontally ($n_{h_{PM}}$) and vertically ($n_{v_{PM}}$) oriented PMs: (a) $n_{h_{PM}} = 3$, $n_{v_{PM}} = 2$, (b) $n_{h_{PM}} = 5$, $n_{v_{PM}} = 4$, and (c) $n_{h_{PM}} = 10$, $n_{v_{PM}} = 9$ and the translational velocity is maintained at 100 m/s. (d) magnetic flux density distributions at the surface of the conductive plate (red dash line).

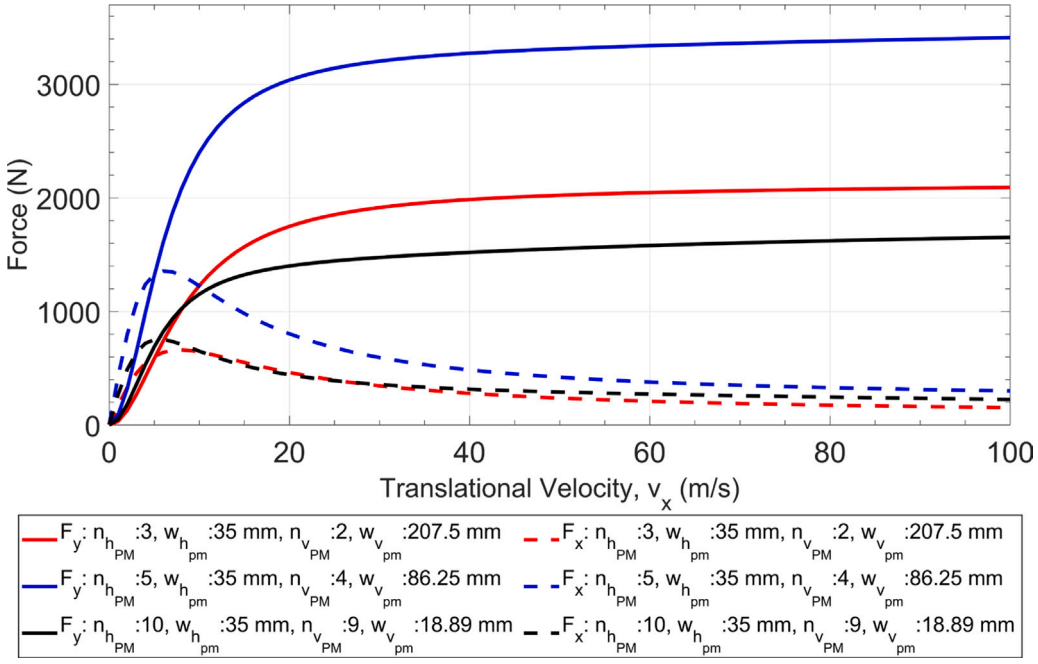


Fig. 6. Lift (F_y) and drag (F_x) forces as a function of the translational velocity for different PM-HA configurations.

$n_{PM} = 19$, the computed values of $F_y - F_x$ were 2040 N, 3224 N, and 1272 N, respectively. A non-monotonic trend is also observed, where the $F_y - F_x$ initially increases with increasing the n_{PM}, reaching a peak around 9 to 11 PMs, before decreasing with further additions. When Eqs. (5)–(7) are collectively considered, it becomes evident that the $F_y - F_x$ is proportional to the pole pitch (τ), the peak magnetic flux density (B_0) and number of pole pairs (ρ), defined as follows:

$$F_y - F_x \propto \frac{B_0^2 w \rho \tau}{\mu_0} \cdot \frac{\sqrt{\tau} - 1}{\sqrt{\tau} + 1} \cdot \frac{1}{\beta\eta + 1} \cdot e^{-\frac{2\pi g}{\tau}} \tag{10}$$

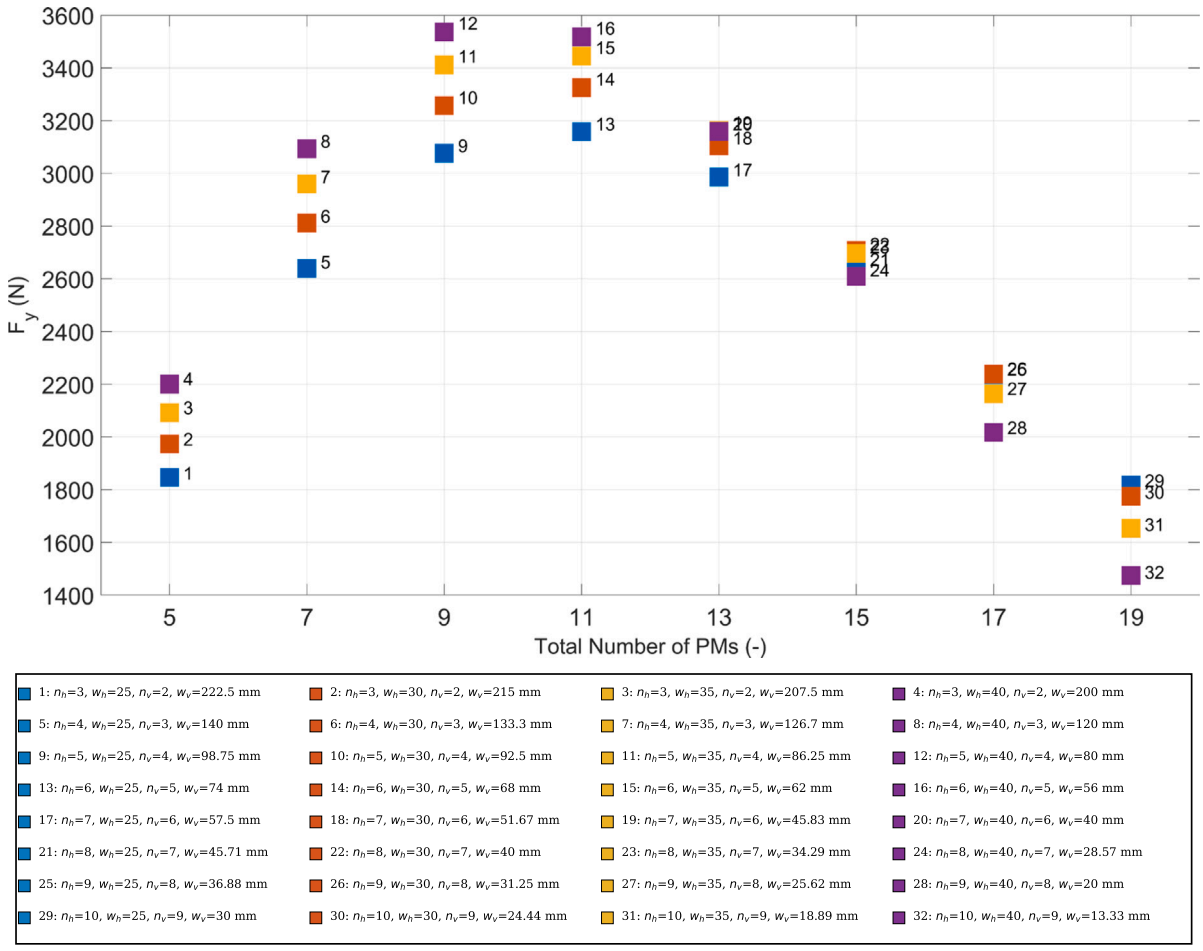


Fig. 7. Variation of the lift force (F_y) at the maximum translational velocity of 100 m/s as a function of the n_{PM} for various PM-HA configurations.

As the n_{PM} increases, the τ (See Fig. 1) decreases. However, in this range, $\rho\tau$ (the product of the number of pole pairs and pole pitch) still grows or remains favorable, enhancing the term $B_0^2 w\rho\tau/\mu_0$. Additionally, the fractional term $\left(\sqrt{\tau}-1\right)/\left(\sqrt{\tau}+1\right)$ increases with τ, but it is bounded and reaches diminishing returns. The exponential term $e^{-2\pi g/\tau}$ decays less as τ increases, supporting higher net force. Together, these effects amplify the net force while n_{PM} increases from 5 to 11. As the n_{PM} increases further from 11 to 19, τ becomes smaller, causing a sharper decay in the exponential term, which dominates and significantly reduces the net force. The fractional term and B_0 also decrease as τ gets smaller, contributing to further reduction (see Fig. 5(d)).

In practical and industrial electrodynamic applications, a high F_y is desirable for effective levitation, while a low F_x is preferred to reduce energy losses due to resistance. Therefore, maximizing the difference $F_y - F_x$ is crucial for optimizing system performance. Configurations 9 and 11 consistently yield the highest $F_y - F_x$ values, indicating that they offer the optimal balance between lift generation and drag reduction. These findings highlight that for an efficient ELS, both the number and size of PMs should be carefully optimized, considering different configurations, rather than simply maximizing them.

The variation of the Lift-to-Drag Ratio (LDR), defined as F_y/F_x, for various PM-HA configurations as a function of the n_{PM} at the maximum v_x value of 100 m/s is shown in Fig. 8. In addition to the $F_y - F_x$ given in Fig. 3, the LDR is another performance indicator in the ELS, reflecting the efficiency of the levitation mechanism. Fig. 8 reveals a clear downward trend in LDR as the n_{PM} increases. Configurations with fewer magnets (i.e. $n_{PM} = 5$ and $n_{PM} = 7$) exhibit the highest LDR values, reaching up to 13.7, suggesting that these arrangements generate significant lift with relatively low resistive drag. A higher LDR means greater efficiency, where strong lift is achieved with minimal drag, which is highly desirable to reduce energy losses and improve system dynamics in applications such as maglev transport. However, a maximum LDR can be achieved by minimizing the drag force even at a lower lift force. This is not suitable for practical Maglev applications where a higher lift force is desired in addition to a lower drag force. Therefore, $F_y - F_x$ is adopted as the optimization objective in this study instead of the LDR.

To make the trade-off between the two performance metrics explicit, the configurations that maximize $F_y - F_x$ and LDR within the parametric set of Figs. 3 and 8 are compared in Table 4. Configuration 12 ($n_{h_{PM}} = 5$, $n_{v_{PM}} = 4$, $w_{h_{PM}} = 40$ mm, $w_{v_{PM}} = 80$ mm) maximizes $F_y - F_x$ at 3224.3 N with $F_y = 3536.4$ N and an LDR of 11.33. Configuration 4 ($n_{h_{PM}} = 3$, $n_{v_{PM}} = 2$, $w_{h_{PM}} = 40$ mm, $w_{v_{PM}} = 200$ mm) maximizes LDR at 13.65 but delivers only $F_y = 2200.2$ N and $F_y - F_x = 2039.0$ N. The configuration selected by the LDR objective therefore provides approximately 38% less lift and 37% less net useful force than the configuration selected by $F_y - F_x$, while configuration 12 still achieves an LDR of 11.33, only $\approx$ 17% below the absolute LDR maximum. A constrained LDR formulation that requires $F_y \geq F_{y,\min}$ would recover the same engineering preference but would introduce the additional manual choice of $F_{y,\min}$. The simple difference $F_y - F_x$ encodes the same trade-off (high lift, low drag) without that auxiliary parameter and is therefore adopted as the optimization objective.

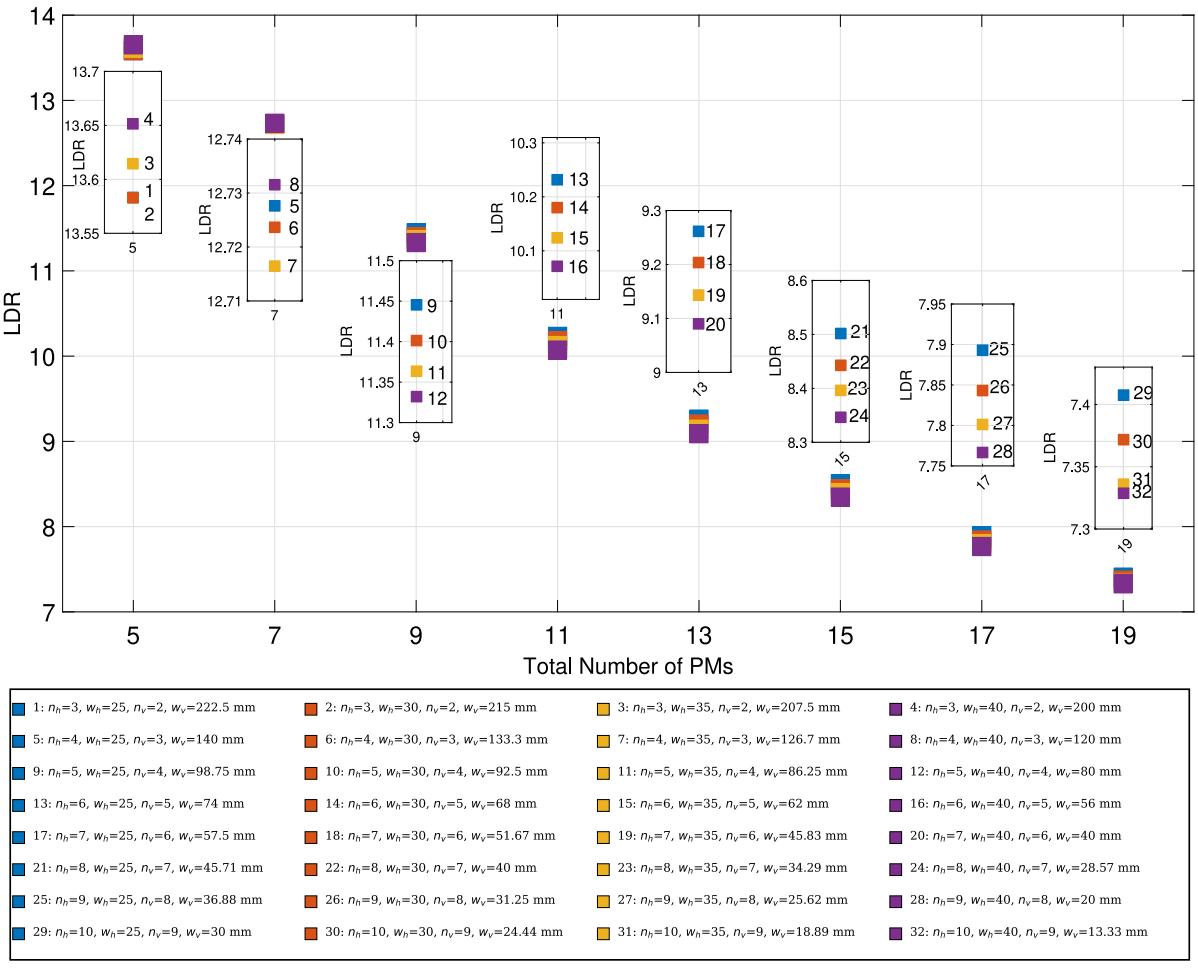


Fig. 8. Variation of the Lift-to-Drag Ratio (LDR) at the maximum translational velocity of 100 m/s as a function of the n_{PM} for various PM-HA configurations.

Table 4
Head-to-head comparison of Conf. 4 and Conf. 12 at v_x = 100 m/s, t_{pl} = 7 mm, and $\sigma = 5 \times 10^7$ S/m.

Quantity	Conf. 4 (LDR_{max})	Conf. 12 ($(F_y - F_x)_{max}$)
$n_{h_{PM}}$	3	5
$n_{v_{PM}}$	2	4
$w_{h_{PM}}$ (mm)	40	40
$w_{v_{PM}}$ (mm)	200	80
Total PMs	5	9
F_y (N)	2200.2	3536.4
F_x (N)	161.2	312.1
$F_y - F_x$ (N)	2039.0	**3224.3**
LDR	**13.65**	11.33

3.3. Optimization results

The optimal configuration of the PM–HA was determined through the defined optimization problem in Section 2.2. The J_z in the conductive plate and the associated A_z at the maximum v_x value of 100 m/s is presented in Fig. 9(a) while F_y and F_x as a function of the v_x is shown in Fig. 9(b) for the optimum configuration. Fig. 9(c) illustrates B_x, B_y magnetic flux density distributions of the optimum configuration and configuration 11 (See Figs. 9(b) and 7).

As shown in Fig. 9(b), the F_y rapidly increases with the increasing v_x, peaking at approximately 3172 N around 21 m/s before gradually saturating and stabilizing at 3550 N at 100 m/s. The F_x shows a peak at 1297 N around 6 m/s, then decreases swiftly, reaching a final value of 279 N at 100 m/s. By comparing the optimum configuration with configuration 11 in Fig. 5(b), one can see that the F_y of the optimum configuration is larger than that of configuration 11, while the F_x shows the opposite behavior. The maximum J_z value of the optimum configuration and configuration 11 are 1.89×10^8 A/m^2 and 2.21×10^8 A/m^2, respectively. Although the J_z value of the optimum configuration is smaller than that of configuration 11, it shows a higher F_y due to its higher B_{norm}, as shown in Figs. 5 and 9(d). In addition, the lower F_x of the optimum configuration compared with configuration 11, in contrast to its higher F_y, can be explained by the lower B_y and higher B_x values (Fig. 9(c)) of the optimum configuration according to the Lorentz force ($F_y = \int J_z \cdot B_x \, dA$; $F_x = \int J_z \cdot B_y \, dA$).

The problem defined in Eq. (9) was solved with the population-based GWO algorithm over 10 independent runs with different random seeds, the mean design parameters are reported in Table 5 (vertical-PM-width standard deviation 0.048 mm, $\approx$ 0.06%). The optimized PM–HA configuration consists of 4 horizontally aligned permanent magnets each 74.00 mm wide and 3 vertically stacked magnets each 74.67 mm wide. In general, this optimization result represents the balance between the structural and electromagnetic properties of PM-HA and the material properties of the conductive plate to obtain the maximum $F_y - F_x$ value.

3.4. Sensitivity to operating temperature and air gap

The parametric and optimization studies were conducted at a fixed plate conductivity of 5×10^7 S/m and a fixed air gap of 25 mm. In service, both quantities deviate from their nominal values: resistive heating of the conductive plate reduces its electrical conductivity, and

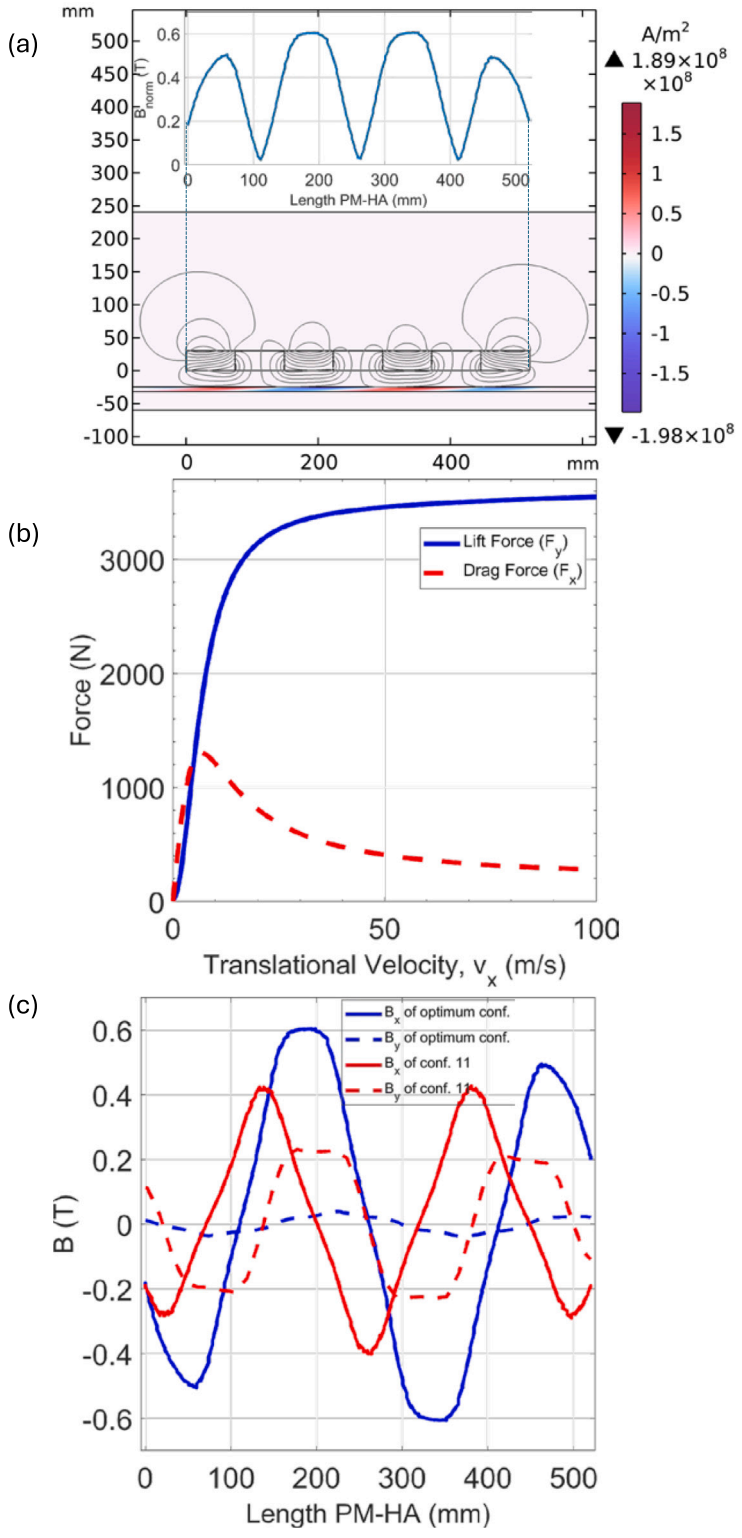


Fig. 9. The results of optimum configuration. (a) z-component of the current density (J_z) in the conductive plate and magnetic vector potential (A_z) at a translational velocity of 100 m/s, (b) Lift (F_y) and drag (F_x) forces as a function of the translational velocity, and (c) B_x, B_y magnetic flux density distributions of the optimum configuration and configuration 11. Inset figure in (a) shows the normalized magnetic flux density distribution of the optimum PM-HA configuration.

dynamic vertical perturbations of the vehicle alter the air gap. The sensitivity of the reported results to these two operating variables is therefore quantified in this subsection.

The effect of operating temperature was evaluated by sweeping the plate conductivity according to the linear model $\sigma(T) = \sigma_0/(1 + \alpha(T - T_{\text{ref}}))$ with $\sigma_0 = 5.998 \times 10^7$ S/m, $\alpha = 3.9 \times 10^{-3}$ K^{-1}, and $T_{\text{ref}} = 20$ °C over $T \in \{20, 40, 60, 80, 100\}$ °C at the optimum geometry and $v_x = 100$ m/s. The results are reported in Table 6. The lift force is remarkably robust to temperature-induced conductivity loss: F_y decreases by only 1.0% between 20 °C and 100 °C. The drag force, in contrast, increases

Table 5
The optimum design parameters for the PM-HA electrodynamic levitation system.

Design parameters	Symbols	Unit	Optimum value
Conductive plate thickness	t_{pl}	mm	7
Horizontal PM width	$w_{h_{PM}}$	mm	74
Vertical PM width	$w_{v_{PM}}$	mm	74.67
Electrical conductivity of the plate	σ	S/m	5×10^7
Number of horizontal PMs	$n_{h_{PM}}$	–	4
Number of vertical PMs	$n_{v_{PM}}$	–	3

Table 6
Temperature-dependent electromagnetic forces at the optimum geometry ($n_{h_{PM}}=4$, $n_{v_{PM}}=3$, $w_{h_{PM}}=74$ mm, $w_{v_{PM}}=74.67$ mm, $t_{pl}=7$ mm, $\sigma_{\text{ref}}=5\times10^7$ S/m at 20 °C) as a function of operating temperature, following the conductivity model $\sigma(T)=\sigma_0/(1+\alpha(T-T_{\text{ref}}))$ with $\sigma_0=5.998\times10^7$ S/m, $\alpha=3.9\times10^{-3}$ K^{-1}, and $T_{\text{ref}}=20$ °C at $v_x=100$ m/s. Columns ΔF_y and ΔF_x report the percentage change relative to the 20 °C reference point.

Temperature (°C)	F_y (N)	F_x (N)	ΔF_y (%)	ΔF_x (%)
20	3549.03	278.55	–	–
40	3539.26	289.10	−0.27	+3.78
60	3530.23	299.71	−0.53	+7.59
80	3521.77	310.45	−0.77	+11.45
100	3513.76	321.33	−1.00	+15.36

by 15.4% over the same range. This behavior follows from the skin depth in Eq. (7): as the conductivity decreases with temperature, the skin depth η grows, the induced eddy currents penetrate deeper into the plate, and the drag term $\beta\eta/(\beta\eta+1)$ in Eq. (6) increases while the lift term $1/(\beta\eta+1)$ in Eq. (5) decreases only marginally. From an engineering perspective, the levitation capability of the optimized system is therefore bounded over the expected thermal range, while the higher drag at elevated temperature must be tolerated as additional resistive loss.

The sensitivity to the air gap was evaluated by computing F_y, F_x, F_y-F_x, and the LDR over $g\in\{20,25,30\}$ mm at six representative configurations spanning the design space (configurations 8, 9, 10, 11, 12, and 16 of Fig. 3) at $v_x=100$ m/s. The results are reported in Table 7. Both forces decrease steeply with the gap, consistent with the exponential decay term $e^{-2\beta g}$ in Eqs. (5) and (6); for configuration 12, F_y falls from 4647.3 N at 20 mm to 2725.3 N at 30 mm. The ranking of the configurations, however, is essentially preserved across the gap range. Configuration 12, which maximizes F_y-F_x at the nominal gap of 25 mm, remains the best at 25 mm and 30 mm, and at 20 mm it is second only to configuration 16 by approximately 4%. The LDR is nearly insensitive to the air gap, varying by less than 3% over the ±5 mm range for every configuration, and improves slightly with increasing gap because the drag decays marginally faster than the lift. The configuration selected at the nominal gap is therefore not an artifact of that particular operating point. As additional engineering information, the vertical stiffness at the operating point, estimated from the finite-difference slope $-\partial F_y/\partial g$ around 25 mm at configuration 12, is approximately 192 N/mm.

4. Conclusions

This study proposed and implemented an FEA-driven optimization approach, integrated with a population-based algorithm, to enhance the electromagnetic performance of a permanent magnet Halbach array (PM-HA)-based electrodynamic levitation (EDL) system. The electromagnetic behavior of the system was rigorously modeled using a high-fidelity 2D FEA model, which incorporated magnetoquasistatic field interactions, the AC/DC Module, Rotating Machinery, Magnetic (RMM) physics, material definitions, boundary conditions, and mesh configurations. The primary design objective was to maximize the net force difference between the lift force (F_y) and drag force (F_x), under practical constraints such as geometric limitations, magnetic array configurations, and material manufacturability. Each design configuration generated during the optimization was independently solved using the defined FEA model. This modeling approach was deliberately chosen over the data-driven surrogate modeling approach to closely emulate realistic physical phenomena, including current distributions, magnetic vector potential, and magnetic flux density.

A comprehensive parametric analysis involving different PM-HA configurations revealed that the lift performance exhibits non-monotonic behavior with respect to the n_{PM} indicating the existence of an optimal n_{PM} for maximizing the lift force, beyond which the benefit of additional magnets diminishes. For configurations with PM numbers of 5, 9, and 19, the values of the net force difference (F_y-F_x) were calculated as 2040 N, 3224 N, and 1272 N, respectively. Specifically, configurations with 9 and 11 PMs produced the best net force difference.

The optimization results identified a configuration consisting of 4 horizontally arranged PMs (each 74.00 mm wide) and 3 vertically arranged PMs (each 74.67 mm wide), paired with a thickness of 7 mm conductive plate with conductivity of $5.0\times10^7 S/m$. This configuration achieved a maximum lift force of 3550 N and a minimum drag force of 279 N at the v_x value of 100 m/s. The optimum configuration with

Table 7
Air-gap sensitivity of the lift force, drag force, net force, and lift-to-drag ratio at six representative configurations of Fig. 3 for $g\in\{20,25,30\}$ mm at $v_x=100$ m/s, $t_{pl}=7$ mm, and $\sigma=5\times10^7$ S/m.

Conf.	g (mm)	$n_{h_{PM}}$	$w_{h_{PM}}$ (mm)	$n_{v_{PM}}$	$w_{v_{PM}}$ (mm)	F_x (N)	F_y (N)	F_y-F_x (N)	LDR
8	20	4	40	3	120	312.82	3891.3	3578.48	12.439
8	25	4	40	3	120	242.94	3093.0	2850.06	12.732
8	30	4	40	3	120	192.57	2502.1	2309.53	12.993
9	20	5	25	4	98.75	359.99	4025.5	3665.51	11.182
9	25	5	25	4	98.75	268.77	3076.2	2807.43	11.445
9	30	5	25	4	98.75	204.62	2378.8	2174.18	11.625
10	20	5	30	4	92.5	381.78	4286.4	3904.62	11.227
10	25	5	30	4	92.5	285.66	3256.9	2971.24	11.401
10	30	5	30	4	92.5	217.43	2511.8	2294.37	11.552
11	20	5	35	4	86.25	399.68	4478.8	4079.12	11.206
11	25	5	35	4	86.25	300.27	3412.1	3111.83	11.363
11	30	5	35	4	86.25	228.64	2629.1	2400.46	11.499
12	20	5	40	4	80	414.33	4647.3	4232.97	11.216
12	25	5	40	4	80	312.07	3536.4	3224.33	11.332
12	30	5	40	4	80	238.01	2725.3	2487.29	11.450
16	20	6	40	5	56	488.00	4905.2	4417.20	10.052
16	25	6	40	5	56	349.26	3517.5	3168.24	10.071
16	30	6	40	5	56	252.69	2568.0	2315.60	10.163

7 PMs ($n_{PM} = 7$) resulted in a lower n_{PM} compared to configuration 12 ($n_{PM} = 9$), which had the highest $F_y - F_x$ value among all defined configurations.

The findings of this work emphasize that optimal levitation performance in PM-HA-based EDL systems arises not from simply maximizing the n_{PM} or their dimensions, but rather from achieving a careful balance among PM size, conductive geometry, magnetic flux density, and induced current pathways. The proposed FEA-driven, population-based optimization methodology thus provides a robust and scalable framework for designing efficient, high-performance electrodynamic suspension systems suitable for future maglev transport and contactless propulsion applications.

CRediT authorship contribution statement

Erkan Caner Ozkat: Writing – review & editing, Writing – original draft, Visualization, Software, Methodology, Investigation, Formal analysis, Data curation, Conceptualization. **Murat Abdioglu:** Writing – review & editing, Writing – original draft, Software, Conceptualization, Investigation, Validation, Investigation. **U. Kemal Ozturk:** Writing – review & editing, Writing – original draft, Conceptualization, Investigation, Validation, Project administration.

Declaration of competing interest

The authors declare that they have no known competing financial interests or personal relationships that could have appeared to influence the work reported in this paper.

Acknowledgments

This study was supported by the Scientific and Technological Research Council of Turkey (TUBITAK) under project number 122F432 and Karadeniz Technical University Scientific Research Projects Coordination Unit under project numbers FDK-2024-16025 and FBA-2024-11081.

References

[1] Y. Xu, Z. Zhao, S. Yin, Z. Long, Real-time performance optimization of electromagnetic levitation systems and the experimental validation, IEEE Trans. Ind. Electron. 70 (3) (2022) 3035–3044, http://dx.doi.org/10.1109/TIE.2022.3167154.

[2] F. Li, Y. Sun, J. Xu, Z. He, G. Lin, Control methods for levitation system of EMS-type maglev vehicles: An overview, Energies 16 (7) (2023) 2995, http://dx.doi.org/10.3390/en16072995.

[3] L. Hao, Z. Huang, F. Dong, D. Qiu, B. Shen, Z. Jin, Study on electrodynamic suspension system with high-temperature superconducting magnets for a high-speed maglev train, IEEE Trans. Appl. Supercond. 29 (2) (2018) 1–5, http://dx.doi.org/10.1109/TASC.2018.2881688.

[4] M. Flankl, T. Wellerdieck, A. Tüysüz, J.W. Kolar, Scaling laws for electrodynamic suspension in high-speedtransportation, IET Electr. Power Appl. 12 (3) (2018) 357–364, http://dx.doi.org/10.1049/iet-epa.2017.0480.

[5] Y. Chen, W. Zhang, J.Z. Bird, S. Paul, K. Zhang, A 3-D analytic-based model of a null-flux halbach array electrodynamic suspension device, IEEE Trans. Magn. 51 (11) (2015) 1–5, http://dx.doi.org/10.1109/TMAG.2015.2444331.

[6] K. Halbach, Design of permanent multipole magnets with oriented rare earth cobalt material, Nucl. Instrum. Methods 169 (1) (1980) 1–10, http://dx.doi.org/10.1016/0029-554X(80)90094-4.

[7] L. Beauloye, B. Dehez, Permanent magnet electrodynamic suspensions applied to maglev transportation systems: A review, IEEE Trans. Transp. Electrification 9 (1) (2022) 748–758, http://dx.doi.org/10.1109/TTE.2022.3193296.

[8] H. Mollahasanoglu, M. Abdioglu, U.K. Ozturk, H.I. Okumus, E. Coskun, A. Gencer, Numerical investigation of EDS maglev systems in terms of performance and cost for different PMs-aluminum rail arrangements, J. Supercond. Nov. Magn. 38 (1) (2025) 52, http://dx.doi.org/10.1007/s10948-024-06899-z.

[9] T. Kublin, L. Grzesiak, P. Radziszewski, M. Nikoniuk, Ł. Ordyszewski, Reducing the power consumption of the electrodynamic suspension levitation system by changing the span of the horizontal magnet in the halbach array, Energies 14 (20) (2021) 6549, http://dx.doi.org/10.3390/en14206549.

[10] Z. Guo, D. Zhou, Q. Chen, P. Yu, J. Li, Design and analysis of a plate type electrodynamic suspension structure for ground high speed systems, Symmetry 11 (9) (2019) 1117, http://dx.doi.org/10.3390/sym11091117.

[11] S. Xiao, K. Zhang, G. Liu, Y. Jing, J.K. Sykulski, Optimal design of a for middle-low-speed maglev trains, Open Phys. 16 (1) (2018) 168–173, http://dx.doi.org/10.1515/phys-2018-0024.

[12] J. Liu, T. Cao, Z. Deng, H. Shi, L. Liang, X. Wu, S. Jiang, Damping characteristics improvement of permanent magnet electrodynamic suspension by utilizing the end-effect of onboard magnets, Electr. Eng. 106 (1) (2024) 15–29, http://dx.doi.org/10.1007/s00202-023-01959-4.

[13] S. Fu, M. Chi, A. Shu, J. Liu, S. Zhang, H. Shi, Z. Deng, Dynamic study on a passive damping scheme for permanent magnet electrodynamic suspension vehicle utilizing onboard magnets end effects, in: Actuators, 14, (7) MDPI, 2025, p. 344, http://dx.doi.org/10.3390/act14070344.

[14] Y. Jiang, Y. Deng, P. Zhu, M. Yang, F. Zhou, Optimization on size of halbach array permanent magnets for magnetic levitation system for permanent magnet maglev train, IEEE Access 9 (2021) 44989–45000, http://dx.doi.org/10.1109/ACCESS.2021.3058124.

[15] Z. Deng, W. Zhang, Y. Chen, X. Yang, C. Xia, J. Zheng, Optimization study of the halbach permanent magnetic guideway for high temperature superconducting magnetic levitation, Supercond. Sci. Technol. 33 (3) (2020) 034009, http://dx.doi.org/10.1088/1361-6668/ab6ec0.

[16] Z. Deng, J. Wang, J. Zheng, Y. Zhang, S. Wang, An efficient and economical way to enhance the performance of present HTS maglev systems by utilizing the anisotropy property of bulk superconductors, Supercond. Sci. Technol. 26 (2) (2012) 025001, http://dx.doi.org/10.1088/0953-2048/26/2/025001.

[17] P. Yang, Y. Sun, Y. Luo, H. Ou, Stability simulation and analysis of maglev vehicle at different speed based on UM, Mechatron. Intell Transp. Syst 2 (1) (2023) 42–52, http://dx.doi.org/10.56578/mits020105.

[18] E.C. Ozkat, M. Abdioglu, U.K. Ozturk, Machine learning driven optimization and parameter selection of multi-surface HTS maglev, Phys. C: Supercond. Appl. 616 (2024) 1354430, http://dx.doi.org/10.1016/j.physc.2023.1354430.

[19] R. Talukdar, S. Talukdar, Dynamic analysis of high-speed maglev vehicle–guideway system: an approach in block diagram environment, Urban Rail Transit 2 (2) (2016) 71–84, http://dx.doi.org/10.1007/s40864-016-0039-8.

[20] Y. Yang, W. Zeng, W.-s. Qiu, T. Wang, Optimization of the suspension parameters of a rail vehicle based on a virtual prototype kriging surrogate model, Proc. Inst. Mech. Eng. Part F: J. Rail Rapid Transit 230 (8) (2016) 1890–1898, http://dx.doi.org/10.1177/095440971561721.

[21] E.C. Ozkat, Photodiode signal patterns: Unsupervised learning for laser weld defect analysis, Processes 13 (1) (2025) 121, http://dx.doi.org/10.3390/pr13010121.

[22] E.C. Ozkat, Vibration data-driven anomaly detection in UAVs: A deep learning approach, Eng. Sci. Technol. an Int. J. 54 (2024) 101702, http://dx.doi.org/10.1016/j.jestch.2024.101702.

[23] G. Yalcin-Ozkat, R.H. Ersan, M. Ulger, S.T. Ulger, S. Burmaoglu, I. Yildiz, O. Algul, Design, synthesis, and computational studies of benzimidazole derivatives as new antitubercular agents, J. Biomol. Struct. Dyn. 41 (7) (2023) 2667–2686, http://dx.doi.org/10.1080/07391102.2022.2036241.

[24] Z. Qiu, S. Han, J. Na, C. Wang, Vertical suspension optimization for a high-speed train with pso intelligent method, Comput. Intell. Neurosci. 2021 (1) (2021) 1526792, http://dx.doi.org/10.1155/2021/1526792.

[25] F. Safaei, A.A. Suratgar, A. Afshar, M. Mirsalim, Characteristics optimization of the maglev train hybrid suspension system using genetic algorithm, IEEE Trans. Energy Convers. 30 (3) (2015) 1163–1170, http://dx.doi.org/10.1109/TEC.2014.2388155.

[26] A. Mughees, S.A. Mohsin, Design and control of magnetic levitation system by optimizing fractional order PID controller using ant colony optimization algorithm, IEEE Access 8 (2020) 116704–116723, http://dx.doi.org/10.1109/ACCESS.2020.3004025.

[27] J. Luo, Z. Su, L. Cui, J. Li, Z. Zhu, G. Ma, Electromagnetic modelling and ripple suppression of asymmetrical ground coil integrated with propulsion, levitation and guidance for EDS train, IEEE Trans. Energy Convers. 38 (1) (2022) 713–723.

[28] Y. Hu, Z. Long, J. Zeng, Z. Wang, Analytical optimization of electrodynamic suspension for ultrahigh-speed ground transportation, IEEE Trans. Magn. 57 (8) (2021) 1–11, http://dx.doi.org/10.1109/TEC.2022.3210478.

[29] S. Mirjalili, S.M. Mirjalili, A. Lewis, G.W. Optimizer, Advances in engineering software, Renew. Sustain. Energy Rev. 69 (2014) 46–61, http://dx.doi.org/10.1109/TMAG.2021.3082686.

[30] Y. Hou, H. Gao, Z. Wang, C. Du, Improved grey wolf optimization algorithm and application, Sensors 22 (10) (2022) 3810, http://dx.doi.org/10.3390/s22103810.

[31] I. Rahimi, A.H. Gandomi, F. Chen, E. Mezura-Montes, A review on constraint handling techniques for population-based algorithms: from single-objective to multi-objective optimization, Arch. Comput. Methods Eng. 30 (3) (2023) 2181–2209, http://dx.doi.org/10.1007/s11831-022-09859-9.

[32] H. Faris, I. Aljarah, M.A. Al-Betar, S. Mirjalili, Grey wolf optimizer: a review of recent variants and applications, Neural Comput. Appl. 30 (2) (2018) 413–435, http://dx.doi.org/10.1007/s00521-017-3272-5.